

Single Crystals of Single-Walled Carbon Nanotubes Formed by Self-Assembly

R. R. Schlittler,¹ J. W. Seo,^{1,2} J. K. Gimzewski,^{1*†} C. Durkan,³
M. S. M. Saifullah,³ M. E. Welland³

We report the self-assembly of single crystals of single-walled carbon nanotubes (SWCNTs) using thermolysis of nano-patterned precursors. The synthesis of these perfectly ordered, single crystals of SWCNTs results in extended structures with dimension on the micrometer scale. Each crystal is composed of an ordered array of tubes with identical diameters and chirality, although these properties vary between crystals. The results show that SWCNTs can be produced as a perfect bulk material on the micrometer scale and point toward the synthesis of bulk macroscopic crystalline material.

Carbon nanotubes have been the subject of intense research since their discovery in 1991 (1). SWCNTs have attracted particular attention because of the wide range of potential applications from structural materials with extraordinary mechanical properties (2) to nanoelectronic components (3) that may allow Moore's Law to be circumvented (4). SWCNTs can also act as probe tips for scanning probe microscopy (5), with the added advantage that the apex may be chemically functionalized. Other proposed applications of nanotubes include high-sensitivity microbalances (6), gas detectors (7, 8), and hydrogen energy storage devices (9). The use of SWCNTs in field-emission mode for displays (10, 11), as electrodes for organic light-emitting diodes (12), and as tiny tweezers for nanoscale manipulation (13) has substantial future technological potential.

One of the most desirable aims of carbon nanotube fabrication is to form large uniform and ordered nano- and microstructures and to eventually bulk materials of SWCNTs. SWCNTs are traditionally synthesized by laser ablation of carbon rods (14) or a direct-current arc discharge between carbon electrodes in an inert gas environment (15). For both methods, the addition of a small quantity of metal catalyst (Co, Ni, Fe, or Mo) increases the yield of SWCNTs (16). To date, the resulting material consists of an entangled and poorly ordered mat or "spa-

ghetti" of SWCNTs, although individual tubes can be several hundreds of micrometers long. Furthermore, the structure of individual tubes varies widely from zigzag, armchair, or chiral forms, which coexist in the material (17). More recently, chemical vapor deposition has been used in combination with nanofabricated catalytic patterning (18) or templating (19) to direct the growth of individual SWCNTs on substrates. However, ordered arrays beyond short sections of ordered SWCNTs of tens of tubes have not yet been produced (20). Likewise, chirality and diameter cannot yet be controlled. Here we report the synthesis of crystals containing millions of well-aligned ordered SWCNTs, all of which are physically identical. Such control is of paramount importance for many applications because the physical properties of the tubes, such as electrical conductivity, are extremely structure sensitive (21).

Crystals of SWCNTs were produced by a method involving nanoscale patterning of solid-state precursor materials. Controlled mixtures of C₆₀ molecules and nickel were evaporated through nanometer-scale apertures onto a molybdenum substrate. The resulting structures were then thermolysed under vacuum in the presence of a magnetic field. A combination of electron diffraction, high-resolution transmission electron microscopy (HRTEM) and electron energy loss spectroscopy (EELS) confirms that the structures produced are almost perfect rod-like crystals of SWCNTs preferentially oriented normal to the surface.

The precursor material from which the nanotubes are grown consists of a heterostructure composed of alternate layers of C₆₀ molecules and nickel thermally evaporated from an Oxford Instruments EC0-4 hearth source. The material was deposited through a shadow mask consisting of several thousand apertures (22) having a diameter of 300 nm and a pitch of 1 μm. Six or seven Ni and C₆₀ layers with individual thicknesses of 10 to 20 nm were depos-

ited. This method of deposition generates small nucleation sites that appear essential for the subsequent self-assembly of the SWCNT crystals. No mask is necessary if the material is deposited on a rough-faceted surface, but fewer tubes are produced in preference to disordered platelets. During evaporation at a pressure of 10⁻⁹ torr onto a room-temperature solid substrate of thermally oxidized Si or a Mo TEM grid, electromechanical shuttering combined with an in situ quartz crystal microbalance to monitor deposition rates ensured that both C₆₀ and Ni could be evaporated sequentially to produce the desired structure. This produces a pillar of material at a specific surface site determined by the relative position of the aperture and surface (Fig. 1A). This method of controlled evaporation through a mask was previously shown to produce 60-nm-wide structures of variable shape when the mask was moved with sub-nanometer precision during the evaporation process (23). The choice of substrate is critical because both C₆₀ and Ni can diffuse at high temperatures, and the aim is to constrain both materials within the original 300-nm-diameter evaporation area. Some success was achieved with the silicon dioxide substrates, but the best results were obtained with a molybdenum substrate either in the form of a grid for subsequent TEM investigation or as a solid film sputtered onto a silicon wafer.

After evaporation of the C₆₀/Ni pillars, the substrates were heated to 950°C in a vacuum of 10⁻⁶ torr for times varying from a few minutes to an hour. The resulting nanotubes were found to preferentially grow normal to the surface when the substrate was immersed in a ~1.5 T magnetic field oriented parallel to the surface normal during heat treatment. Directing the self-assembly and organization of the SWCNT crystals in this way provides the possibility of controlling the growth direction by changing the orientation of the external magnetic field.

In a scanning electron microscope (SEM) image of some of the structures produced by this method (Fig. 1B), four rod-shaped structures of approximately the same diameter and length with curved end caps are seen growing normal to the surface. This image is typical of the structures produced, although the length and width of the rods vary. To confirm that the rods were composed of carbon nanotube bundles, they were grown on molybdenum TEM grids so that EELS (to confirm the chemical composition) and electron diffraction (to confirm the molecular structure) could be carried out.

The EELS spectrum of one of the rod-shaped crystals (Fig. 2) was acquired in a VG 501HB STEM operating at 100 kV with a dispersion of 0.1 eV per channel. The spectrum of the carbon-K edge shows an intense pre-peak at 285 eV, just below the main absorption threshold. This pre-peak is a char-

¹IBM Research, Zurich Research Laboratory, Säumerstrasse 4, CH-8803 Rüschlikon, Switzerland. ²Institut de Physique, Université de Neuchâtel, CH-2000 Neuchâtel, Switzerland. ³Nanoscale Science Laboratory, Department of Engineering, University of Cambridge, Cambridge CB2 1PZ, UK.

*To whom correspondence should be addressed. E-mail: gim@chem.ucla.edu

†Present address: Department of Chemistry and Biochemistry, University of California at Los Angeles, 607 Charles E. Young Drive East, Box 951569, Los Angeles, CA 90095-1569, USA.

acteristic of the transitions to π^* states in sp^2 -bonded carbon, suggesting that graphite-like sheets are present in the sample. The spectrum closely resembles previous EELS spectra of carbon nanotubes (24) and confirms that they are indeed made of carbon. Nickel was only detected in the EELS spectra during the growth phase of the nanotubes, with no evidence of either nickel or molybdenum in the fully grown nanotubes.

HRTEM studies were performed in a JEOL 4000FX microscope operating at 400 kV. Detailed diffraction analysis was carried out in a 200-kV JEOL 2010 microscope. Nanotube rods grown on the Mo grid were less uniform in size than those grown on SiO_2 ; diameters varied between 40 and 900 nm and lengths reached up to 2 μm (Fig. 3A). These rods were straight and preferentially aligned parallel to the Mo-grid plane, making it impossible to image the tubes along the tube axis. All tubes were found to be SWCNTs. The wall diameters in a given rod are remarkably uniform. From one rod to another they range from about 1.4 to 2.3 nm, consistent with values observed elsewhere (25). There is an inverse correlation between wall and rod diameters: small wall diameters are predominantly observed in large-diameter rods, whereas large wall diameters are found in small-diameter rods. No evidence for multi-wall carbon nanotubes or isolated single-wall tubes was found. This was based on detailed wall thickness measurements as well as on the absence of empty core regions within the rods. For small rods, beam damage at 400 kV was substantial, as also observed by others (15, 26). However, for the larger rods, we observed that damage proceeds much more slowly, with no obvious modifications over an exposure time of about 1 to 2 min.

An electron diffraction pattern from a rod composed of SWCNTs of diameter 1.66 nm (Fig. 3B) shows sharp diffraction spots, indicating a highly ordered structure due to the regular arrangement of tubes in the rod, which must be considered as a periodically ordered crystal of SWCNTs. This periodicity leads to strong reflections in the diffraction pattern; as a result, the typical streaking of spots perpendicular to the tube axis, which appear because of the curvature of the graphene sheet, almost disappear. Such streaking was only observed in crystals with a much smaller diameter. The electron diffraction pattern of Fig. 3B can be considered as a set of sharp diffraction spots lying in two principle directions. The first direction, normal to the long axis of the tubes within the crystal, is a direct measure of the tube diameter, once an inter-tube spacing is assumed. If a range of tube diameters existed, this would correspond to a range of positions, resulting in streaks in the diffraction reflection. This clearly is not observed, indicating that the SWCNTs in a crystal have identical diameters defined by the reciprocal width of the relevant diffraction spot. The second diffraction direction provides a measure

of the chirality of the tubes in the crystal. An isolated single nanotube with some arbitrary chirality will produce two related diffraction spots: one for the chiral angle associated with the graphene sheet spacing at an angle α to the tube axis, corresponding to the projection of the top of the tube, and one at angle $-\alpha$ for the bottom half of the tube. Here the tube axis is assumed to be normal to the incident electron beam. For a rope or crystal composed of a number of SWCNTs with a range of chiral angles, the diffraction spots associated with the chirality would form arcs (20). The fact that we only see one diffraction spot implies only one chiral angle. Therefore, we conclude that monodispersed crystals of SWCNTs are formed. The two primary directions indicated in Fig. 3B correspond to half the SWCNT

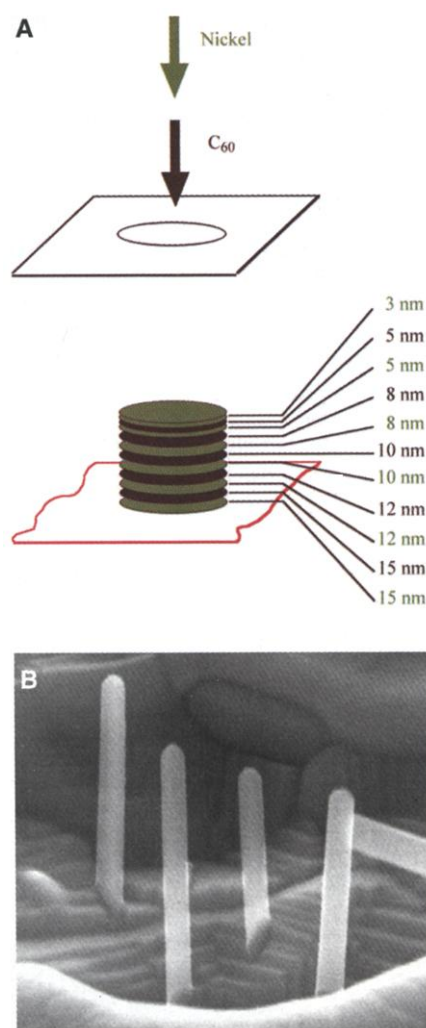


Fig. 1. (A) Schematic of the deposition process by which C_{60} and Ni are alternately evaporated through a 300-nm-diameter mask to produce the required multilayer structure. (B) SEM image of rods of SWCNTs grown on a Mo substrate. The rods in this image have a diameter of ~ 50 nm, although generally there are a range of diameters and shapes on a Mo substrate.

wall width of 0.829 nm and, orthogonal to this, a spacing of 0.24 nm corresponding to the spacing of the graphite hexagons. The weak super-reflections have a spacing that corresponds to twice that of 0.24 nm.

There is a simple, commonly used relation between the diameter and helicity of individual nanotubes (20), specified in terms of a roll-up vector (n, m) that arises from considering how a one-atom-thick graphite sheet can be rolled up to produce a nanotube. The diameter d and chiral angle θ are given by

$$d = 0.077(n^2 + nm + m^2)^{1/2} \quad (1a)$$

$$\sin\theta = (3m/2)(n^2 + nm + m^2)^{-1/2} \quad (1b)$$

From Fig. 3B, the chiral angle θ can be deduced to be 30° by considering the simple geometric relation between the 0.24-nm reflection direction, the graphene lattice, and the 0.829-nm tube-radius reflection. This corresponds to an armchair-type tube so that $m = n$. The tube-radius reflection corresponds to a diameter d of 1.658 nm, which is actually equal to $(d + d_t)$, where d_t is the nearest-neighbor carbon-carbon distance between atoms belonging to adjacent tubes. Taking d_t to be 0.34 nm (17, 27), we obtain $n = m = 10$, which is in excellent agreement with the thermodynamically stable SWCNT structure reported previously (14).

Having interpreted the diffraction pattern of Fig. 3B as that of a crystal of SWCNTs with (10,10) chirality, we further corroborate this by simulating the diffraction pattern using the CrystalKit software (28). The kinematic simulation takes a hexagonal crystal of (10,10) SWCNTs as the basis for calculation. We are then able to generate diffraction patterns at varying angles of electron incidence. The pattern of Fig. 3B corresponds to an angle of incidence normal to the long tube axis. In the corresponding calculation (Fig. 3C), the spot marked by

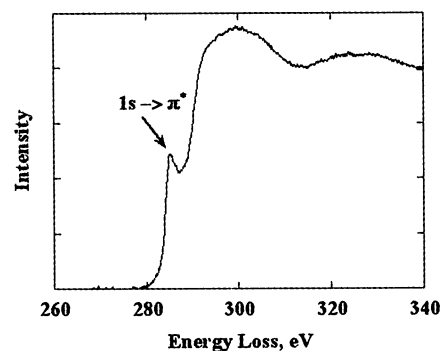


Fig. 2. EELS spectra of a SWCNT crystal grown on a Mo TEM grid. The electron beam was positioned approximately halfway along the length of the crystal to record the spectrum. For all fully formed SWCNT crystals measured, the form of the spectrum was found to be independent of the electron beam position, except at the base of the crystal where a contribution from the substrate was detected.

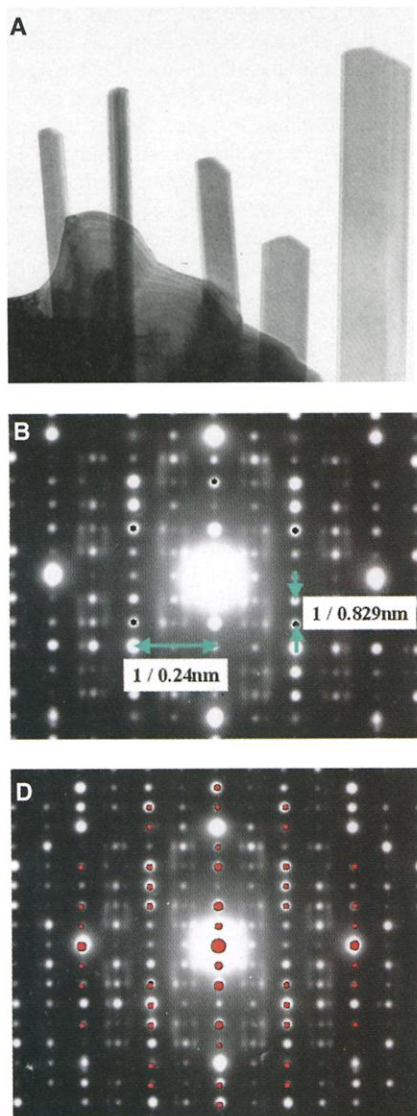
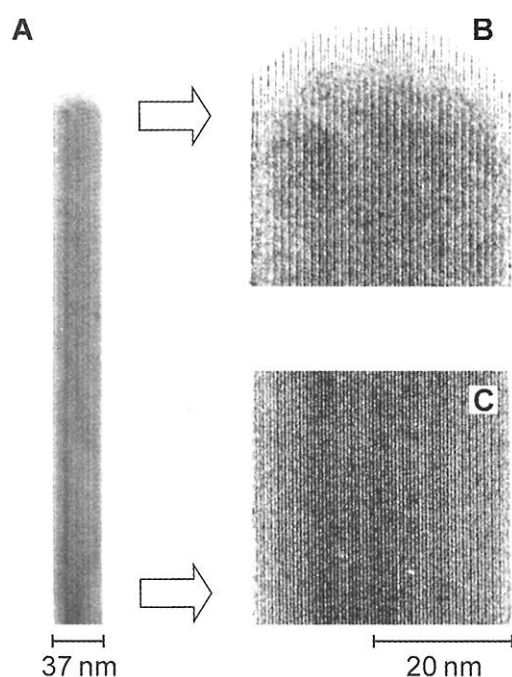


Fig. 4. (A) HRTEM image of a portion of a single SWCNT crystal with a diameter of 37 nm and a length of ~750 nm. (B and C) Detail from the apex and base of the SWCNT crystal, respectively. The visible 1.6-nm lattice spacing originates from the spacing between the individual nanotubes packed on a hexagonal lattice in the direction of the long axis of the crystal. The structural perfection along the entire length is demonstrated by the exact, defect-free order of the internal structure.



arrow 1 is correlated with the lattice spacing perpendicular to the tube axis (half of $1.36 + 0.34 = 1.7$ nm). Arrows 1 and 3 (Fig. 3C) show spots that match perfectly; arrow 2 shows that the spot related to the spacing 0.24 nm is missing. This is a consequence of the limitations of the kinematic simulation; in dynamic diffraction this missing spot will appear. The good match between spot position and intensity can be more clearly seen when the experimental and calculated diffraction patterns are overlaid (Fig. 3D). The simulation is not sufficiently detailed to result in an exact match but nevertheless provides further evidence for our interpretation of the SWCNT crystal structure.

A final structural observation relates to the shape of the individual crystals. Previous observations of SWCNT bundles have demonstrated that the tubes are packed in a hexagonal structure when looking down the end of the bundle. There is then a question as to whether the equilibrium cross-sectional shape of a crystal would be circular or hexagonal or whether it would exhibit a more complex section. A simple argu-

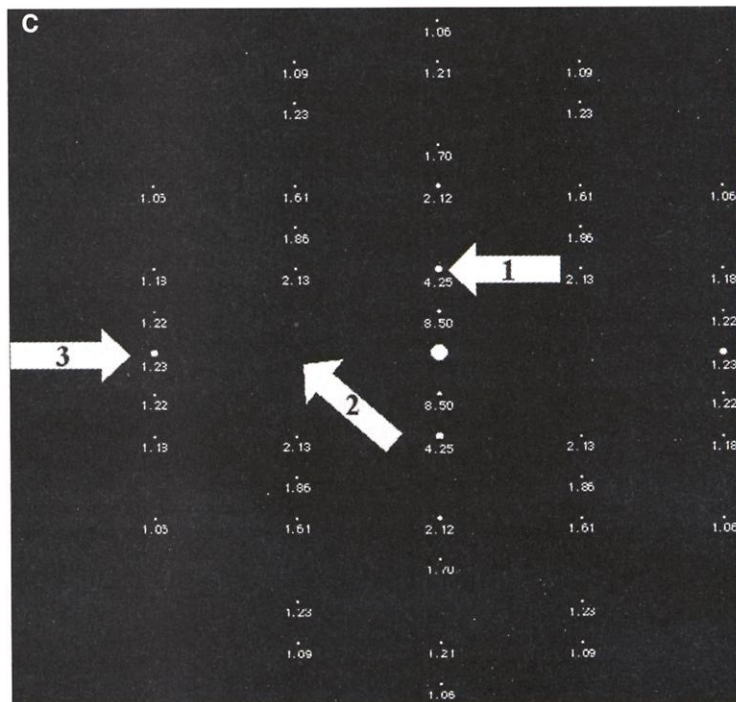


Fig. 3. (A) Bright-field TEM image of five SWCNT crystals growing from the edge of a Mo support grid. (B) Representative electron diffraction pattern of a SWCNT crystal. The reflections corresponding to the radius (0.829 nm) of the individual tubes making up the crystal and the graphene spacing (0.24 nm) are indicated. The graphene spacing corresponds to $\sqrt{3}$ of the carbon-carbon bond spacing of 0.141 nm. (C) Kinematic diffraction simulation of an array of hexagonally packed (10,10) SWCNTs using CrystaKit (28). Arrows 1 to 3 indicate the diffraction spots associated with the tube diameter and chiral directions. Normal incidence of the electron beam is assumed relative to the long axis of the crystal. The numbers indicate the calculated intensities of each diffraction spot. (D) An overlay of (B) and (C), where (B) is in white and (C) is in red, demonstrating the good match between simulation and experiment.

ment based on a hexagonally packed structure of identical SWCNTs would favor a structure whose faces consisted of close-packed SWCNTs. This would include a hexagonal cross section but could equally well be any cross section consisting of 120° facets. We are unable to take a diffraction pattern along the crystal length, but the projected shapes of the crystals and the contrast in the HRTEM images indicate that faceting of the SWCNT crystals does indeed occur as seen at the ends of the crystals in Fig. 3A.

HRTEM investigations were performed on several crystals, including one that is ~750 nm long and ~40 nm in diameter with a curved end cap (Fig. 4A). Higher magnification images show the internal structure at the apex (Fig. 4B) and at the base of the crystal (Fig. 4C). Figure 4B shows the perfect regular arrangement of 1.6-nm-diameter SWCNTs in a bundle with no evidence of inhomogeneity or defect. This structural perfection was a characteristic of all nanotubes produced using this technique.

The perfection of the crystals of SWCNTs and the observation that they are all physically identical within any given crystal containing up to several thousand individual nanotubes are unexpected from the point of view of previous results and synthetic approaches in the field. Nevertheless, the expected, most stable arrangement of a nanotube crystal, as shown here, follows general thermodynamic expectations of a minimum-energy configuration over an extended array of tubes in close contact. Minimization of energy also implies that all tubes be identical and straight, permitting maximization of the van der Waals interactions, minimization of strain, and a hexagonally packed lattice.

Our results provide evidence of faceting of SWCNT crystals. The role of weak forces such as applied magnetic fields and the spatial localization of the reactants appear to be essential to direct the self-assembly process. The approach we have discussed shows that nanostructuring of reactants in the solid-state reaction of C₆₀ and Ni is a key feature to the formation of SWCNTs organized into a bulk crystalline material.

References and Notes

1. S. Iijima, *Nature* **354**, 56 (1991).
2. M. M. J. Treacy, T. W. Ebbesen, J. M. Gibson, *Nature* **381**, 678 (1996).
3. S. J. Tans, R. M. Verschueren, C. Dekker, *Nature* **393**, 40 (1998).
4. "Every 18 months, processing power doubles while cost holds constant," G. Moore, Intel Corporation, 1965.
5. H. Dai, J. H. Hafner, A. G. Rinzler, D. T. Colbert, R. E. Smalley, *Nature* **384**, 147 (1996).
6. Ph. Poncharal, Z. L. Wang, D. Ugarte, W. A. de Heer, *Science* **283**, 1513 (1999).
7. J. Kong et al., *Science* **287**, 622 (2000).
8. P. G. Collins, K. Bradley, M. Ishigami, A. Zettl, *Science* **287**, 1801 (2000).
9. A. C. Dillon et al., *Nature* **386**, 377 (1997).
10. Q. H. Wang et al., *Appl. Phys. Lett.* **72**, 2912 (1998).
11. S. Fan et al., *Science* **283**, 512 (1999).

12. C. J. Lee et al., *Appl. Phys. Lett.* **75**, 1721 (1999).
13. P. Kim, C. M. Lieber, *Science* **286**, 2148 (1999).
14. A. Thess et al., *Science* **273**, 483 (1996).
15. S. Iijima, T. Ichihashi, *Nature* **363**, 603 (1993).
16. D. S. Bethune et al., *Nature* **363**, 605 (1993).
17. See, for example, X. F. Zhang et al., *J. Cryst. Growth* **130**, 368 (1993).
18. M. Terrones et al., *Nature* **388**, 52 (1997).
19. J. Li, C. Papadopoulos, J. M. Xu, M. Moskovits, *Appl. Phys. Lett.* **75**, 367 (1999).
20. L. Henrard et al., *Eur. Phys. J. B* **13**, 661 (2000).
21. N. Hamada, S. I. Sawada, A. Oshiyama, *Phys. Rev. Lett.* **68**, 1579 (1992).
22. J. Brugger et al., *Microelectron. Eng.* **53**, 403 (2000).
23. R. Lüthi et al., *Appl. Phys. Lett.* **75**, 1314 (1999).
24. R. Kuzo, M. Terauchi, M. Tanaka, *Jpn. J. Appl. Phys.* **31**, L1484 (1992).
25. R. Saito, G. Dresselhaus, *Physical Properties of Carbon Nanotubes* (Imperial College Press, London, 1998).

26. R. R. Meyer et al., *Science* **289**, 1324 (2000).
27. C.-H. Kiang et al., *Phys. Rev. Lett.* **81**, 1869 (1998).
28. CrystallKit was written by Roar Kilaas, Total Resolution, 20 Florida Avenue, Berkeley CA, USA.
29. This work has partially been supported through the European Union and the Swiss Federal Office for Education and Science by the Information Society Technologies—Future Emerging Technology (IST-FET) projects AT-OMS and BUN. We thank J. Brugger for his help in developing the original sieve technology and F. Diederich for useful discussions. J.W.S. acknowledges support by the Swiss National Science Foundation and thanks the Institut für Festkörperforschung (Forschungszentrum Jülich, Germany) for use of the 4000FX microscope.

28 November 2000; accepted 23 March 2001
 Published online 5 April 2001;
 10.1126/science.1057823
 Include this information when citing this paper.

Reaction-Controlled Phase-Transfer Catalysis for Propylene Epoxidation to Propylene Oxide

Xi Zuwei,* Zhou Ning, Sun Yu, Li Kunlan

The epoxidation of olefins with H₂O₂ was performed with a tungsten-containing catalyst. This insoluble catalyst forms soluble active species by the action of H₂O₂, and when the H₂O₂ is used up, the catalyst precipitates for easy recycling. Thus, the advantages of both homogeneous and heterogeneous catalysts are combined in one system through reaction-controlled phase transfer of the catalyst. When coupled with the 2-ethylantraquinone/2-ethylantrahydroquinone redox process for H₂O₂ production, O₂ can be used for the epoxidation of propylene to propylene oxide with 85% yield based on 2-ethylantrahydroquinone without any co-products. This approach avoids the problematic co-products normally associated with the industrial production of propylene oxide.

Propylene oxide is used for making polyurethane, unsaturated resins, surfactants, and other products, and market demand for it has been increasing over the years. Its current worldwide production capacity is around 4.5 million metric tons per year. There are two industrial methods for propylene oxide production: the chlorohydrin method and the Halcon method. In the chlorohydrin method, large amounts of Cl₂ are consumed, which gives rise to serious problems of equipment corrosion and environmental pollution. In the Halcon method, autoxidation of ethylbenzene or isobutane is used to make alkylhydroperoxide, which acts as an oxidant for catalytic epoxidation of propylene to propylene oxide, together with a large amount of co-products. Thus, the Halcon process is a very complicated one and needs heavy capital investment.

Dalian Institute of Chemical Physics, Chinese Academy of Sciences, Zhongshan Road 457, Dalian 116023, People's Republic of China.

*To whom correspondence should be addressed. E-mail: huangw@dicp.ac.cn

The oxidation of propylene to propylene oxide without any co-products in a more environmentally friendly way has been an important objective for many chemists. Although O₂ is an inexpensive and clean oxidant, heterogeneous catalytic epoxidation of propylene with O₂ usually gives poor selectivity because of the high reaction temperature (1, 2). H₂O₂ is also a clean oxidant, and the TS-1 zeolite catalyst for propylene epoxidation with H₂O₂ in methanol solution has high catalytic activity and selectivity (3). Moreover, the TS-1 zeolite can be easily separated and reused. However, this method has not yet been commercialized because of the relatively high cost of H₂O₂ when used to produce a low-priced commodity chemical such as propylene oxide. Some researchers have used the redox reaction of 2-ethylantraquinone (EAQ)/2-ethylantrahydroquinone (EAHQ), with O₂ as the oxidant, to produce H₂O₂ in situ, which then undergoes propylene epoxidation in the presence of TS-1 zeolite (4). However, because of the restriction imposed by the properties of the TS-1 zeolite (5), its reaction medium in the EAQ/EAHQ system is more complicated than that of the normal industrial